



# Fast Prediction of Multiple Parameters Related to Iced Airfoil Based on POD and Kriging Methods

J. Niu<sup>1</sup>, W. Sang<sup>1,2†</sup>, D. Li<sup>1</sup>, Q. Guo<sup>1,3</sup>, A. Qiu<sup>1</sup> and M. Shi<sup>1</sup>

<sup>1</sup> College of Aeronautics, Northwestern Polytechnical University, Xi'an, Shaanxi, 710072, China

<sup>2</sup> Key Laboratory of Icing and Anti/De-icing, China Aerodynamics Research and Development Center, Mianyang, Sichuan, 621000, China

<sup>3</sup> School of Aeronautical Engineering, Civil Aviation Flight University of China, Guanghan, Sichuan, 618300, China

†Corresponding Author Email: [sangweimin@nwpu.edu.cn](mailto:sangweimin@nwpu.edu.cn)

(Received June 19, 2022; accepted September 29, 2022)

## ABSTRACT

Ice accretion threatens aircraft safety. With the wide application of unmanned aerial vehicles (UAVs), the design of ice-tolerant UAVs has become a problem that must be solved. Forty conditions for the continuous/intermittent maximum icing conditions were sampled in Appendix C of Federal Aviation Regulations Part 25. Herein, numerical simulations of icing were performed on an NACA 0009 airfoil for 5, 15, and 30 min, and the ice mass and ice shapes were obtained at different times. Numerical simulations of the aerodynamic characteristics of the iced configuration at 5, 15, and 30 min were conducted, and the coefficients of lift, drag, and pitch moment were obtained. Surrogate models of the ice shape, mass of the ice accretion, lift coefficient, drag coefficient, and pitch moment coefficient at different moments were built based on proper orthogonal decomposition and kriging interpolation. The results demonstrate that the surrogate models accurately predicted the ice shape, ice mass, lift coefficient, drag coefficient, and pitch moment coefficient at different moments. Compared with the numerical simulation results, the maximum relative errors of the ice mass, lift coefficient, drag, and pitch moment predicted by the surrogate models were 7.8%, 3.4%, 3.9%, and 7.6%, respectively. This method can help in designing the ice-tolerant UAVs and envelope determination under icing conditions.

**Keywords:** Ice tolerance; Envelope protection; Icing; POD; Kriging.

## 1. INTRODUCTION

When an aircraft flies through a cloud containing supercooled droplets, ice accretion can occur on the wing surface. Aircraft icing is considered to be one of the most serious hazards affecting flight safety (Smith 1929). Although various efforts have been made to solve icing problems in past decades, ice accretion on aircraft remains a major threat to flight safety (Potapczuk 2013). Significant efforts have been made to avoid icing risks during flights. One of the risk prediction methods is based on the pilot report, through which pilots communicate the current intensity of icing and estimate whether the aircraft can maintain safe operation before entering the reported area. However, this report is ambiguous and subjective (Zeppetelli and Habashi 2012). Bragg *et al.* (2002) developed a smart icing system (SIS). The SIS uses system identification to predict aircraft performance and control changes in icing conditions. Sharma *et al.* (2004) studied a typical autopilot structure for flights under icing conditions and

developed a practical envelope protection scheme. Hossain *et al.* (2003) developed an iced aircraft envelope protection system. Pei *et al.* (2018) developed an approach for the quantitative assessment of the flight risk under icing conditions.

Recently, unmanned aerial vehicles (UAVs) have played an important role in various fields, such as sea ice monitoring (Wang *et al.* 2018), search and rescue (Scherer *et al.* 2015), and icing detection on wind turbines or power lines (Bhola *et al.* 2018). Several UAV missions require operation under harsh weather conditions. However, the icing of UAVs restricts their application. In addition, the available solutions for the de-icing/anti-icing of UAVs are limited (Idris *et al.* 2020).

UAVs must satisfy strict icing safety requirements (Cebeci and Kafyeke 2003). Vukits (2002) stated that the best way to avoid natural icing hazards is to have accurate forecasts, know what conditions lead to natural icing, and accordingly avoid them. Gui *et al.* (2017) noted that boundary protection is

important to guarantee the safety of aircraft and proposed the concept of multiple safety boundaries of iced aircrafts. The safety boundaries in aircraft icing can be divided into boundaries of weather, ice shape, and flight performance.

Guided by this background, a method for icing risk management is proposed. The spatial distribution of icing meteorological conditions in the target area and their changes over time can be obtained using a weather research and forecasting (WRF) model. Various researchers have confirmed that the WRF can accurately predict icing meteorological conditions (Thompson 2019). The icing influence can be determined quickly with the help of the surrogate models. Thus, the safety envelope or graded safety zones under icing conditions in the target zones can be derived.

The numerical simulation of ice accretion includes the solution of the airflow field, calculation of water droplet impingement characteristics, calculation of icing, grid displacement, and continuous iteration until the icing time is reached; therefore, the time cost of the numerical simulation of icing is relatively large. Consequently, quickly obtaining the iced configuration and the change in aerodynamic characteristics under icing conditions is essential for quickly determining the safety boundary. A reduced-order model based on proper orthogonal decomposition (POD) can quickly obtain the required results while ensuring accuracy. In fluid dynamics and turbulence analyses, POD is used to replace the Navier–Stokes equations (Berkooz *et al.* 1993). Jaiswal *et al.* (2022) used POD to explain airfoil tonal noise amplitude reduction. Kim *et al.* (2022) studied the influence of varying the frequency of a synthetic jet on flow separation over an airfoil using POD. Radmanesh *et al.* (2021) used POD to estimate wildfires and plan UAV paths.

The basic principle of POD involves extracting a series of orthogonal basis vectors from an existing sample set. The original sample space can be described by a linear superposition of these vectors. Some low-energy modes can then be discarded according to the required accuracy to form a low-order subspace, which can be quickly reconstructed from the sample space. For conditions that are not included in the sample space, the results can also be predicted quickly with the linear combinations of the vectors and the associated coefficients. The coefficients can be obtained using surrogate models.

A variety of surrogate models have been developed, including response surface models, kriging models, radial basis function models, neural networks, and support vector regression. The kriging model provides the predicted value of the unknown function and also the error estimate of the predicted value, which is a significant feature that distinguishes the kriging model from other methods. The kriging model is attracting increasing attention from researchers because of its good approximation ability for nonlinear functions and its unique error estimation function. Kriging interpolation was proposed by the South African engineer Krige (1951) and has been widely used in various fields.

Optimization with kriging interpolation has been applied to structural optimization design (He *et al.* 2014) and high-speed train shape design (Yao *et al.* 2013). Pellissier *et al.* (2012) optimized an anti-icing chamber using POD and kriging methods. Liu *et al.* (2019) predicted the ice shapes on airfoils using the POD and kriging methods.

The present study focused on fast prediction of the ice shape and the variation in ice mass and the coefficients of the lift, drag, and pitch moment with the iced configuration. Therefore, surrogate models related to these parameters were constructed based on POD and kriging methods. By utilizing the continuous/intermittent maximum icing conditions in Appendix C of the Federal Aviation Regulations (FAR) Part 25, numerical simulations of icing were performed to obtain the ice shapes and ice mass for 5, 15, and 30 min. Numerical simulations of aerodynamic characteristics were performed on the iced configuration at different moments, and the lift, drag, and pitch moment coefficients were obtained. Based on the data acquired, POD and kriging methods were used to build the surrogate model that can quickly predict the lift coefficient, drag coefficient, pitch moment coefficient, ice shape and ice mass at 5, 15, and 30 min.

## 2. METHOD

Fast prediction of the multiple parameters related to an iced airfoil based on POD and kriging methods includes the following: numerical simulation of ice accretion, which aims to obtain the ice shapes and ice mass at different moments; numerical simulation of the iced configuration to obtain the aerodynamic characteristics at different moments; and the construction of surrogate models based on POD and kriging methods for the ice shape, ice mass, and coefficients of lift, drag, and pitch moment.

### 2.1 Numerical Simulation of Icing

#### 2.1.1 Airflow field calculation

The airflow field is described by the conservation equations for mass, momentum, and energy (Jia 2018). The mass conservation equation is as follows.

$$\frac{\partial \rho_a}{\partial t} + \vec{\nabla} \cdot (\rho_a \vec{V}_a) = 0 \quad (1)$$

where  $\rho_a$  and  $\vec{V}_a$  are the density and velocity of air, respectively. The momentum conservation equation is

$$\frac{\partial \rho_a \vec{V}_a}{\partial t} + \vec{\nabla} \cdot (\rho_a \vec{V}_a \vec{V}_a) = \vec{\nabla} \cdot \sigma^{ij} + \rho_a \vec{g} \quad (2)$$

where  $\sigma^{ij}$  is the stress and can be written as

$$\begin{aligned} \sigma^{ij} &= -\delta^{ij} p_a + \\ &\mu_a \left[ \delta^{jk} \nabla_k v^i + \delta^{ik} \nabla_k v^j - \frac{2}{3} \delta^{ij} \nabla_k v^k \right] \\ &= -\delta^{ij} p_a + \tau^{ij} \end{aligned} \quad (3)$$

$$\tau^{ij} = \mu_a [\delta^{ik} \nabla_k v^j + \delta^{jk} \nabla_k v^i - \frac{2}{3} \delta^{ij} \nabla_k v^k] \quad (4)$$

Here,  $p_a$  and  $\mu_a$  are the static pressure and dynamic viscosity of air, respectively.

The energy conservation equation is

$$\frac{\partial \rho_a E_a}{\partial t} + \vec{\nabla} \cdot (\rho_a \vec{V}_a H_a) = \vec{\nabla} \cdot [\kappa_a (\vec{\nabla} T_a) + v_i \tau^{ij}] + \rho_a \vec{g} \cdot \vec{V}_a \quad (5)$$

where  $E_a$  is total internal energy,  $H_a$  is enthalpy, and  $\kappa_a$  is the thermal conductivity.

### 2.1.2. Calculation of droplet impingement characteristics

There are two main methods to establish the motion equation of supercooled water droplets: the Lagrange and Euler methods. The Lagrange method calculates the stress of the droplets according to Newton's second law. The Euler method regards droplets and air as a homogeneous gas-liquid two-phase flow and establishes the motion equation of water droplets in the Euler coordinate system. In the present study, the Euler method was used to calculate droplet motion. These equations can be written as follows (Jia 2018).

$$\frac{\partial \alpha}{\partial t} + \vec{\nabla} \cdot (\alpha \vec{V}_d) = 0 \quad (6)$$

$$\frac{\partial (\alpha \vec{V}_d)}{\partial t} + \vec{\nabla} [\alpha \vec{V}_d \otimes \vec{V}_d] = \frac{C_d Re_d}{24K} \alpha (\vec{V}_a - \vec{V}_d) + \alpha (1 - \frac{\rho_a}{\rho_d}) + \frac{1}{Fr^2} \quad (7)$$

where  $\alpha$  is the water volume fraction, and  $\vec{V}_d$  is the velocity of the droplets. The first term on the right side of Eq. (7) is the drag acting on the droplets. The drag is related to the droplet Reynolds number, coefficient of drag  $C_d$ , and relative velocity of the air and droplet. The droplet Reynolds number is

$$Re_d = \frac{\rho_a d V_{a,\infty} \|\vec{V}_a - \vec{V}_d\|}{\mu_a} \quad (8)$$

The inertial parameter  $K$  can be calculated by

$$K = \frac{\rho_d d^2 V_{a,\infty}}{18 L_\infty \mu_a} \quad (9)$$

The second term on the right of Eq. (7) represents the buoyancy and gravity forces, which relate to the local Froude number:

$$Fr = \frac{\|\vec{V}_{a,\infty}\|}{\sqrt{L_\infty g_\infty}} \quad (10)$$

The coefficient of drag is calculated by

$$C_D = (24 / Re_d)(1 + 0.15 Re_d^{0.687}) \quad (11)$$

for  $Re_d \leq 1300$   
 $C_D = 0.4$   
 for  $Re_d > 1300$

The water collection coefficient  $\beta$  can be written as

$$\beta = -\alpha \vec{V}_d \cdot \vec{n} \quad (12)$$

Furthermore, the water collected by the surface can be written as

$$\square m_w = \beta \cdot LWC \cdot V_\infty \quad (13)$$

### 2.1.3. Ice accretion model

Figure 1 shows the mass and heat transfer when the water film flows over the surface. On a solid surface, the water is modeled as a thin liquid film, and the film is driven by the shear force to run back (Bourgault *et al.* 2000). During the running-back process, the film may freeze, evaporate, or sublimate according to the thermodynamic conditions.

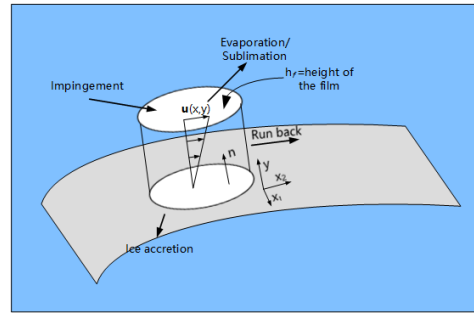


Fig. 1. Schematic of water film on the surface.

The film velocity is a function of  $\mathbf{x} = (x_1, x_2)$  and  $y$ , where  $\mathbf{x} = (x_1, x_2)$  are the coordinates on the surface, and  $y$  is the coordinate normal to the surface. Because the water film is extremely thin, the velocity of the film can be considered to have a linear distribution. Thus, the velocity can be calculated by

$$\vec{V}_f(\mathbf{x}, y) = \frac{y}{h_f} \vec{\tau}_{a,wall}(\mathbf{x}) \quad (14)$$

where  $\vec{\tau}_{a,wall}(\mathbf{x})$  is the shear stress of air. The average velocity across the film thickness can be derived as

$$\bar{\vec{V}}_f(\mathbf{x}, y) = \frac{1}{h_f} \int_0^{h_f} \vec{V}_f(\mathbf{x}, y) dy = \frac{h_f}{2\mu_f} \vec{\tau}_{a,wall}(\mathbf{x}) \quad (15)$$

The mass conservation of the water on the surface can be written as

$$\rho_f \left[ \frac{\partial h_f}{\partial t} + \vec{\nabla} \cdot (\bar{\vec{V}}_f h_f) \right] = \square m_w - \square m_{evap} - \square m_{ice} \quad (16)$$

where the terms on the right of Eq. (16) are the mass of droplet impingement, mass of evaporation, and mass of ice accretion, respectively. The energy conservation of water on the surface can be written as follows.

$$\begin{aligned} \rho_f \left[ \frac{\partial h_f c_f \tilde{T}_f}{\partial t} + \vec{\nabla} \cdot (\vec{V}_f h_f c_f \tilde{T}_f) \right] = \\ [c_f (\tilde{T}_\infty - \tilde{T}_f) + \frac{\|\vec{V}_d\|^2}{2}] V_\infty LWC \beta - \\ L_{evap} m_{evap} + (L_{fusion} - c_s \tilde{T}) m_{ice} + \\ \sigma \varepsilon (T_\infty^4 - \tilde{T}_f^4) - c_h (\tilde{T}_f - \tilde{T}_{ice,rec}) + Q_{anti-ice} \end{aligned} \quad (17)$$

where the first three terms on the right-hand side are the heat transfer generated by the impinging water droplets, evaporation, and ice accretion, respectively. The last three terms are the radiative, convective, and conductive heat fluxes, respectively. Compatibility relations are necessary to close the system of equations.

$$\begin{cases} h_f \geq 0 \\ m_{ice} \geq 0 \\ h_f \tilde{T}_f \geq 0 \\ m_{ice} \tilde{T}_f \leq 0 \end{cases} \quad (18)$$

These inequalities ensure that when the equilibrium temperature is below the freezing point (273.15 K), there is no liquid water, and when the temperature is above 273.15 K, there is no ice.

## 2.2 Numerical Simulation of Aerodynamic Characteristics

After obtaining the ice shapes of the NACA 0009 airfoil at 5, 15, and 30 min under different icing conditions, numerical simulations of the aerodynamic characteristics of the ice configurations were performed. The aerodynamic characteristics of the iced configuration, such as the coefficients of the lift, drag, and pitch moment, were obtained by solving the Navier–Stokes equations, and the Spalart–Allmaras turbulence model was used in the solving process. The semi-implicit method for pressure linked equations algorithm is used to solve the basic equations. The pressure, momentum, turbulent kinetic energy, and energy terms are discretized in a second-order manner. The pressure and momentum relaxation is 0.4, and the convergence accuracy is set to 1e-5. The lift and drag coefficients are monitored during the simulation until the changes in these coefficients are less than 0.0001 and 0.00001, respectively.

## 2.3 Surrogate Model

### 2.3.1 Proper orthogonal decomposition

POD has been applied in various fields. It is a method that reduces the complexity of simulations. POD can

rebuild an intermediate solution using a series of previous solutions or snapshots. The solutions can be expressed as a set of linear combinations of basis functions and coefficients (Sirovich 1987):

$$U_j = \sum_{i=1}^{ns} \alpha_{ij} \cdot \Phi_i \quad (19)$$

The basis functions can be extracted from the eigenvalue problem associated with the cross-correlation matrix, which is related to combined snapshots. Because the vector space is orthonormal, the coefficients are simply the dot product of the corresponding eigenfunction with the snapshot itself. The target solution can be written as a linear combination of the following basis functions:

$$\hat{U} = \sum_{i=1}^{nm \leq ns} \hat{\alpha}_i \cdot \Phi_i \quad (20)$$

### 2.3.2. Kriging interpolation

Kriging interpolation is a method in which the interpolated values are modeled using a Gaussian process governed by the prior covariance. The best unbiased prediction of the intermediate values can be obtained using Kriging interpolation. The prediction of Kriging interpolation includes the global model and localized departures, as follows (Han 2016).

$$y(\mathbf{x}) = f(\mathbf{x}) + Z(\mathbf{x}) \quad (21)$$

where  $y(\mathbf{x})$  is the prediction of the interest  $\mathbf{x}$ ,  $f(\mathbf{x})$  is the approximation function that provides a global model of the design space, and  $Z(\mathbf{x})$  gives the localized deviations with mean zero, variance  $\sigma^2$ , and nonzero covariance. The covariance matrix of  $Z(\mathbf{x})$  can be calculated by

$$Cov[Z(x_i), Z(x_j)] = \sigma^2 \mathbf{R}([\mathbf{R}(x_i, x_j)]) \quad (22)$$

where  $\mathbf{R}$  is a symmetric matrix,  $\mathbf{R}(x_i, x_j)$  is the Gaussian correlation function between any two of the sampled points  $x_i$  and  $x_j$ , and  $\mathbf{R}(x_i, x_j)$  can be calculated by

$$\mathbf{R}(x_i, x_j) = \exp\left(-\sum_{k=1}^n \theta_k \left| \mathbf{x}_k^i - \mathbf{x}_k^j \right|^2\right) \quad (23)$$

where  $\theta_k$  is the unknown correlation parameter used to fit the model, and  $\mathbf{x}_k^i$  and  $\mathbf{x}_k^j$  are the  $k$ th component of the sample points  $x_i$  and  $x_j$ . The predicted estimates,  $\hat{y}(\mathbf{x})$ , of the response  $y(\mathbf{x})$  of  $\mathbf{x}$  can be determined by

$$\hat{y}(\mathbf{x}) = \hat{\beta} + \mathbf{r}^T \mathbf{R}^{-1} (\mathbf{y} - \mathbf{f} \hat{\beta}) \quad (24)$$

where  $\mathbf{y}$  and  $\mathbf{f}$  are both column vectors of length,  $\mathbf{y}$  contains the sample values of the response, and  $\mathbf{f}$  is filled with ones when  $f(\mathbf{x})$  is taken as a constant. Here,  $\mathbf{r}^T$  can be calculated by

$$\mathbf{r}^T(x) = [\mathbf{R}(x, x_1), \mathbf{R}(x, x_1) \dots \mathbf{R}(x, x_n)]^T \quad (25)$$

and  $\hat{\beta}$  is estimated by

$$\hat{\beta} = (f^T \mathbf{R}^{-1} f)^{-1} f^T \mathbf{R}^{-1} y \quad (26)$$

The variance  $\hat{\sigma}^2$  is estimated by

$$\hat{\sigma}^2 = [(y - f \hat{\beta}) \mathbf{R}^{-1} (y - f \hat{\beta})] / n_s \quad (27)$$

where  $f(x)$  is assumed to be a constant,  $\hat{\beta}$ . The estimation of  $\theta_k$  can be determined by

$$\max \Phi(\theta_k) = - \left[ n_s \ln(\hat{\sigma}^2) + \ln |\mathbf{R}| \right] / 2 \quad (28)$$

where  $\hat{\sigma}^2$  and  $|\mathbf{R}|$  are the functions of  $\theta_k$ . The optimal kriging model can be obtained by solving Eq. (28). In the present study, kriging was achieved using the OODACE toolbox.

### 3. VALIDATION

#### 3.1 Validation of the Icing Simulation

Ice accretion is affected by the temperature, liquid water content (LWC), velocity, median volume diameter (MVD) of the droplets, etc. There are always two types of ice accretion on aircraft: rime ice and glazed ice. Rime ice generally forms at temperatures below 264.15 K, and glazed ice forms between 264.15 and 273.15 K. The surface of rime ice is generally rough, and its shape is generally consistent with the leading edge of the airfoil. Glazed ice is relatively transparent, and ice horns always form on the leading edge of the airfoil. Glazed ice poses a greater threat to aircrafts. Therefore, two different icing conditions were chosen to validate the icing simulation, and the ice shapes obtained by the simulation were compared with the results in the literature (Shin and Bond 1992). Table 1 lists the icing conditions used to validate the numerical simulation of icing.

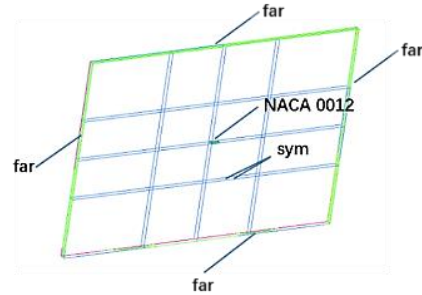
**Table 1** Icing conditions used in the icing numerical simulation validation cases

No.	1	2
V, m/s	67.05	67.05
AOA, °	4	4
MVD, μm	20	20
LWC, g/m <sup>3</sup>	1	1
T, K	267.05	244.75
t, min	6	6

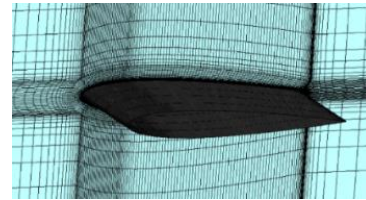
Figures 2 and 3 show the boundary conditions and mesh of NACA 0012, and the number of grids is 300,000.

Figure 4 shows a comparison of ice shape between the experimental and numerical simulation results of the two validation cases. The ice shapes obtained by numerical simulation are consistent with the

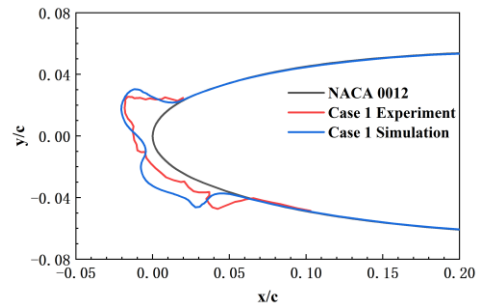
experiments, and the numerical simulation can efficiently capture the ice horn on the leading edge of the airfoil. Therefore, it is considered that the numerical simulation of icing can accurately obtain the ice shape.



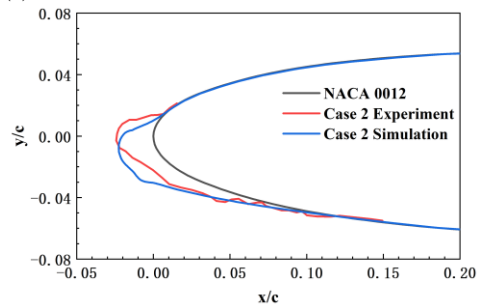
**Fig. 2.** Computational domain of NACA 0012.



**Fig. 3.** Grid of NACA 0012.



(a) Glazed ice



(b) Rime ice

**Fig. 4.** Comparison of ice shapes between the numerical simulation and experimental result.

#### 3.2 Validation of Aerodynamic Characteristics Simulation

The aerodynamic characteristics of the iced configuration were numerically analyzed, and the coefficients of the lift, drag, and pitch moment obtained were compared with the experimental results. Owing to the greater impact on the

aerodynamics of glazed ice, in the present work, the aerodynamic characteristics of the configuration with glazed ice were numerically simulated and compared with previous results (Bragg and Coirier 1986).

Figure 5 shows the ice shape of NACA 0012 with glazed ice. Table 2 lists the icing conditions of NACA 0012.

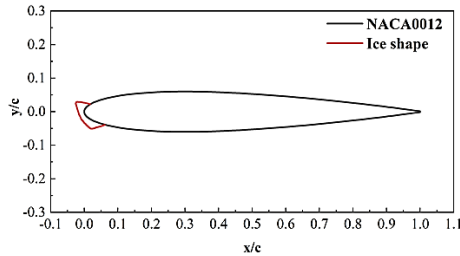


Fig. 5. Glazed ice shape of NACA 0012.

Table 2 Conditions used in the aerodynamic characteristics validation cases

Chord, m	Ma	Re
0.5334	0.12	1.5E+6

Figure 6 shows a comparison of the coefficients of lift, drag, and pitch moment between the simulated results and experimental results of NACA 0012 with glazed ice. The figure indicates that the numerical simulation of aerodynamic characteristics can yield accurate coefficients of lift, drag, and pitch moment of the iced configuration.

#### 4. RESULTS AND DISCUSSION

##### 4.1 Numerical Simulation of Icing and Aerodynamic Characteristics

Appendix C of FAR Part 25 illustrates the continuous/intermittent maximum icing conditions. Forty icing conditions for each of the continuous and intermittent maximum icing conditions were obtained using optimal Latin hypercube sampling (OLHS). Figure 7 shows the samples under continuous/intermittent maximum icing conditions. Table 3 lists the flight conditions of the NACA 0009.

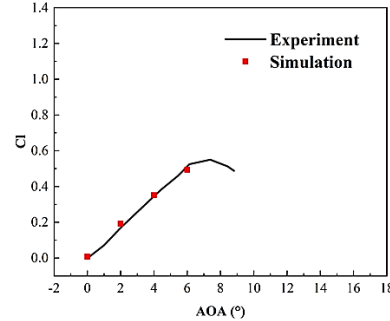
Table 3 Flight conditions of NACA 0009

Parameters	Values
Chord, m	1
AOA, °	3
Indicate airspeed, m/s	10

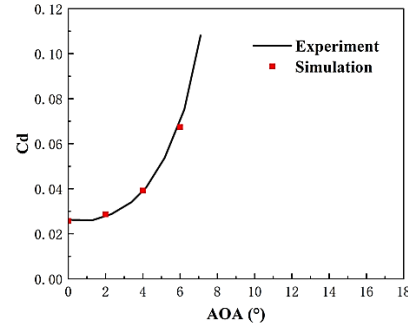
Numerical simulations of ice accretion were performed for the 80 samples for 5, 15, and 30 min, and the ice shapes and ice mass at different moments were obtained. Thereafter, the aerodynamic characteristics were simulated numerically for the iced configurations. Some of the results are illustrated below. The icing conditions for these cases are listed in Table 4.

Table 4 Icing conditions of part samples

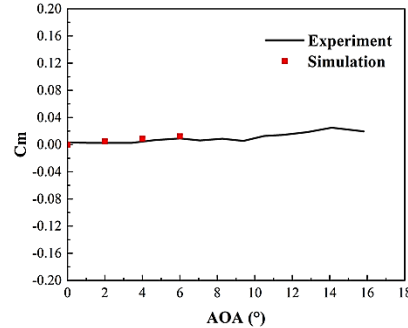
No.	T, K	H, m	MVD, $\mu\text{m}$	LWC, $\text{g/m}^3$
1	260.70	4800	25.25	0.2099
2	237.95	7739	24.87	0.5105
3	268.48	1990	23.09	2.0867



(a) Lift coefficient



(b) Drag coefficient

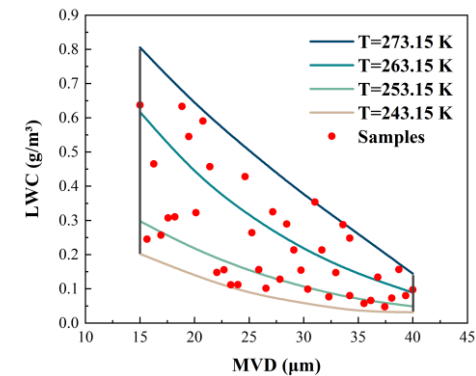


(c) Pitch moment coefficient

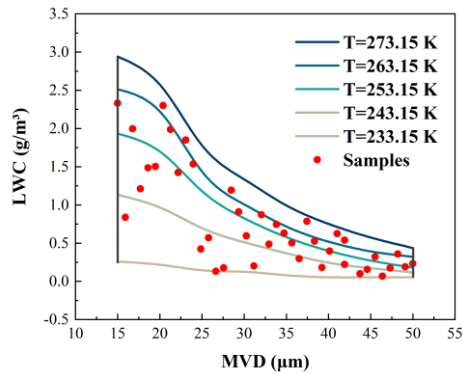
Fig. 6. Comparison of lift, drag, and pitch moment coefficients of NACA 0012 with glazed ice shape.

Figure 8 shows the ice shapes at 5, 15, and 30 min for cases 1–3. The figures indicate that ice accumulates continuously on the leading edge of the NACA 0009 with increasing time. The temperatures of cases 1 and 2 are lower, the ice shapes are rime ice, and the ice shapes are generally consistent with the leading edge of the NACA 0009. The temperature in case 3 is higher, and the ice shape is glazed ice. An ice horn can be seen on the upper leading edge of the NACA 0009. Compared with the ice shapes in Figure 4, the ice shapes in Fig. 8 appear more regular. This is because the ice accretion is a continuous accumulation process and the ice generated has an impact on the airflow field and the droplet

impingement characteristics, while these changes also affect the ice formation. Compared with the icing condition in Fig. 4, the greatest difference in the icing condition in Fig. 8 is its lower velocity. The indicated velocity is only 10 m/s. Eq. (13) shows that the amount of collected water shown in Fig. 4 is larger than that in Fig. 8 for the same time, indicating that the ice formed is larger and the impact on the airflow field and droplet impingement characteristics is greater than those in Fig. 8. Therefore, the ice shapes appear more regular.



(a) Continuous maximum icing conditions



(b) Intermittent maximum icing conditions

**Fig. 7. Samples of continuous/intermittent maximum icing conditions.**

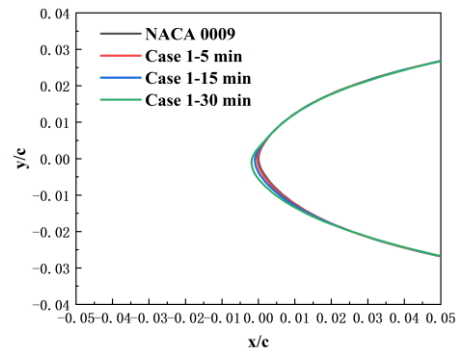
Tables 5 and 6 list the ice mass and the coefficients of lift, drag, and pitch moment of cases 1–3 at different moments. Table 5 shows that the ice mass increases with an increase in time. Different ice types have different effects on the aerodynamic characteristics. Cases 1 and 2 are rime ice. The ice has little effect on the coefficients of lift and drag owing to the shape consistency of the rime ice. Case 3 is glazed ice. The glazed ice results in a reduction in lift and an increase in drag. However, ice accretion in all the cases leads to an increase in the pitch moment coefficient.

**Table 5 Ice mass of the cases 1–3 at different moments (kg/m)**

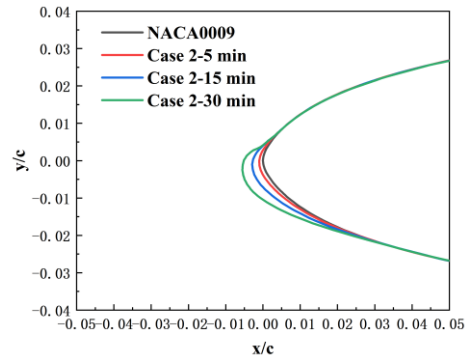
No.	5 min	15 min	30 min
1	6.3630E-03	1.9366E-02	3.8433E-02
2	2.2047E-02	6.6198E-02	1.2968E-01
3	3.0559E-02	9.3401E-02	1.9179E-01

**Table 6 Lift/drag/pitch moment coefficients of cases 1–3 at different moments**

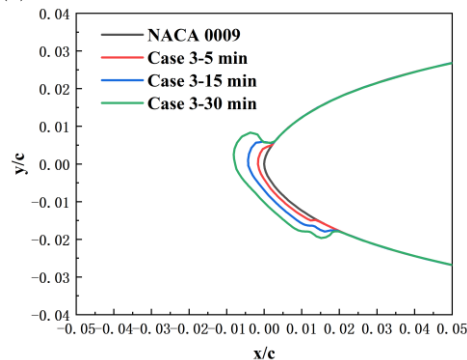
	No.	5 min	15 min	30 min
Cl (*0.1)	1	3.386	3.383	3.382
	2	3.386	3.387	3.381
	3	3.357	3.337	3.218
Cd (*0.01)	1	1.282	1.285	1.279
	2	1.313	1.314	1.315
	3	1.269	1.363	1.413
Cm (*0.001)	1	2.642	2.728	2.784
	2	2.185	2.289	2.584
	3	3.824	4.260	10.337



(a) case 1



(b) case 2

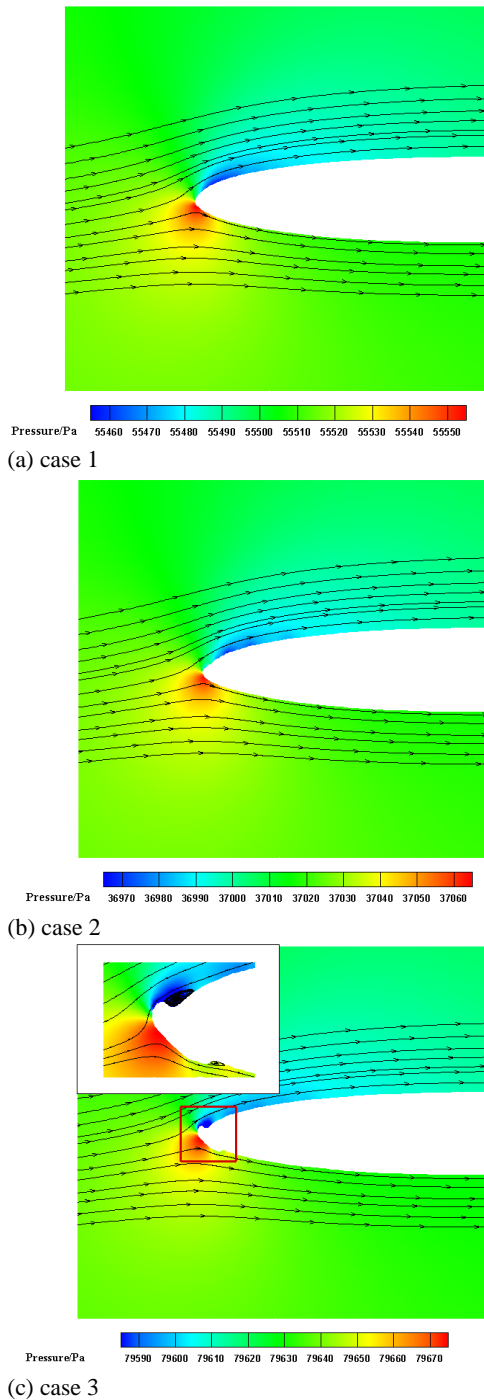


(c) case 3

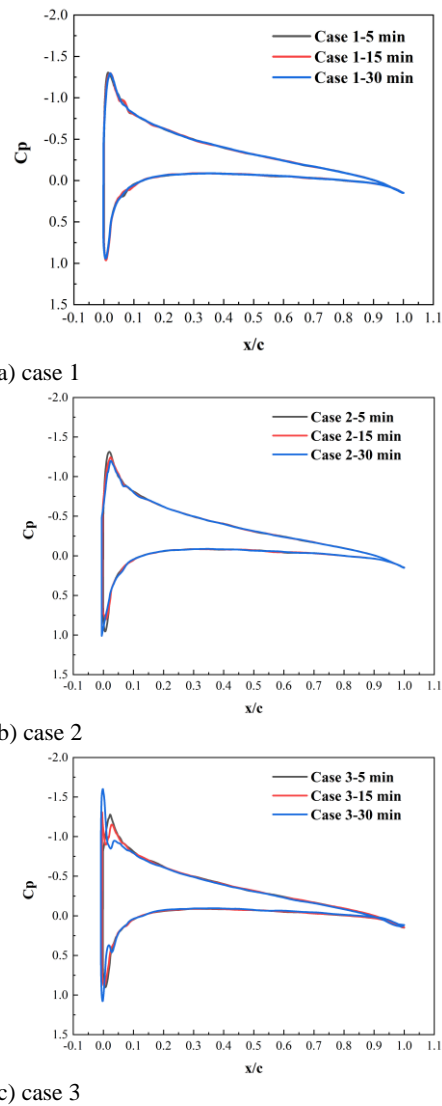
**Fig. 8. Ice shapes of cases 1–3 at 5, 15, and 30 min.**

Figure 9 illustrates the pressure contours and streamlines of the cases 1–3 at 30 min. Because the ice accretion of cases 1 and 2 is small, the ice shape does not significantly change the shape of the leading edge; therefore, the streamline does not change

considerably as well. In contrast, case 3 has a larger ice shape that changes the shape of the leading edge more, forming horns on the upper and lower surfaces of the leading edge of the wing, and resulting in separation in the area behind the horns. Figure 10 shows the pressure coefficient distribution of the three cases at 5, 15, and 30 min. Clearly, case 3 has a drastic change in the pressure coefficient at the leading edge of the upper and lower airfoils because of the separation at 30 min, leading to a large change in its pitch moment at 30 min.



**Fig. 9. Pressure contour and streamlines at 30 min.**



**Fig. 10. Pressure coefficient distribution at different moments.**

#### 4.2 Prediction of the Surrogate Model

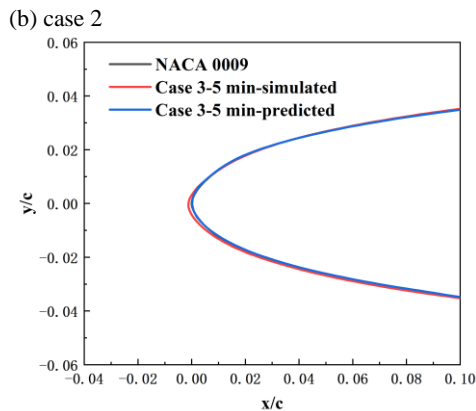
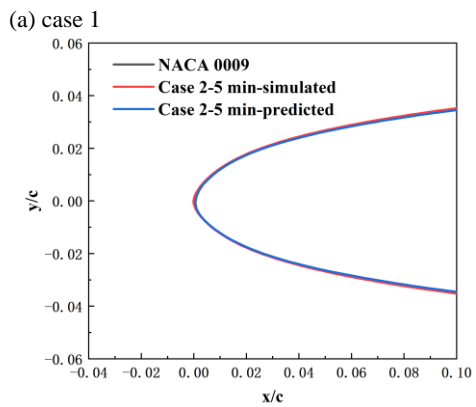
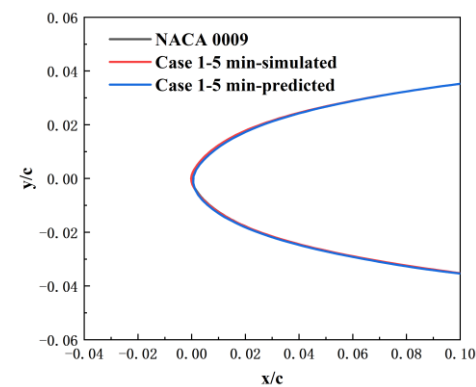
Numerical simulations of ice accretion were performed for 80 samples for 5, 15, and 30 min, and the ice mass and ice shapes were obtained at different moments. Numerical simulations of the aerodynamic characteristics of the NACA 0009 with iced configurations were performed, and the lift, drag, and pitch moment coefficients were obtained. Based on the obtained data, surrogate models were established based on POD and kriging interpolation to predict the operating conditions at nonoperating points. Three cases were selected to validate the accuracy of the surrogate model. Table 7 lists the conditions for these cases.

**Table 7 Conditions of validation cases.**

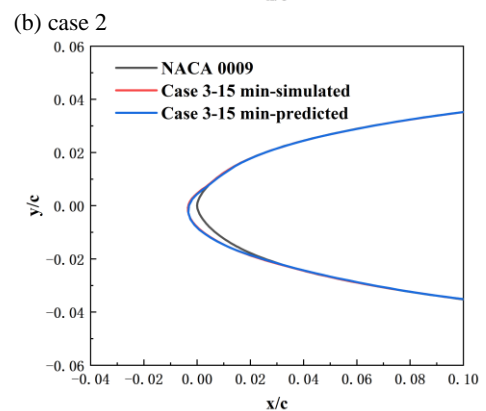
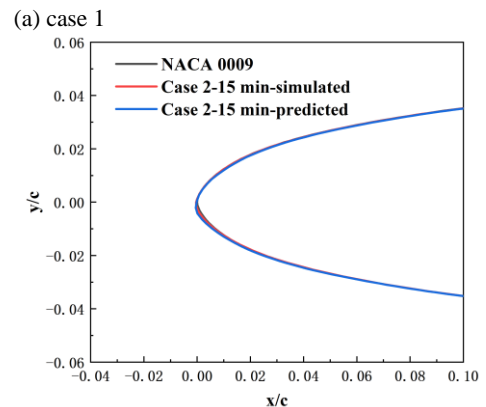
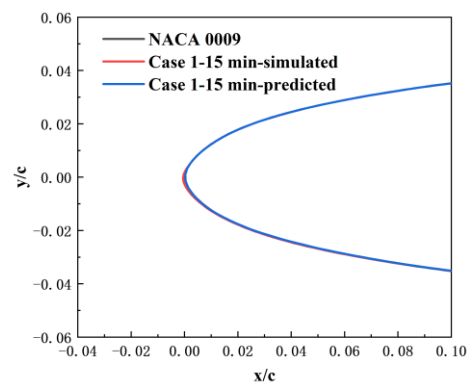
No.	T, K	H, m	MVD, $\mu\text{m}$	LWC, $\text{g/m}^3$
1	255	3000	25	0.1500
2	265	1000	20	0.1978
3	250	5000	30	0.6992

Figures 11–13 illustrate the ice shape comparison of the results between the surrogate models and icing numerical simulation at 5, 15, and 30 min. The ice accretion of the cases at 5 min was slight for the short icing time, as shown in Fig. 11. The results of the surrogate models and numerical simulation are nearly the same. As time progresses, ice accumulates on the leading edge of the NACA 0009. Figure 12 shows the ice shapes at 15 min, comparing the surrogate models and numerical simulation. Figure 12 shows that the ice shapes of the surrogate model match well with the ice shapes of the numerical simulation. Ice accumulates increasingly over time, leading to large changes near the leading edge, as shown in Fig. 13(c). However, the ice shape predicted by the surrogate models is consistent with the simulation results. Compared with Fig. 8, the

biggest difference between the conditions in Fig. 13 is that the LWC is lower. Ice accretion is affected by temperature, LWC, MVD, speed, etc. According to a previous study (Makkonen 1981), ice accretion can be divided into glazed ice and rime ice, which correspond to wet and dry growth, respectively. The regimes of dry and wet growth and the critical LWC can be found in the literature. When the LWC exceeds the critical LWC, the result is glazed ice. The critical LWC is a function of the velocity, temperature, and maximum droplet collection coefficient. For cases 1 and 2 in Fig. 8 and cases 1–3 in Fig. 13, the growth type is dry growth, indicating the formation of rime ice. For case 3 in Fig. 8, the growth is wet growth, resulting in the formation of glazed ice.



(a) case 1  
(b) case 2  
(c) case 3  
**Fig. 11. Ice shape comparison of the cases at 5 min.**



(a) case 1  
(b) case 2  
(c) case 3  
**Fig. 12. Ice shape comparison of the cases at 15 min.**

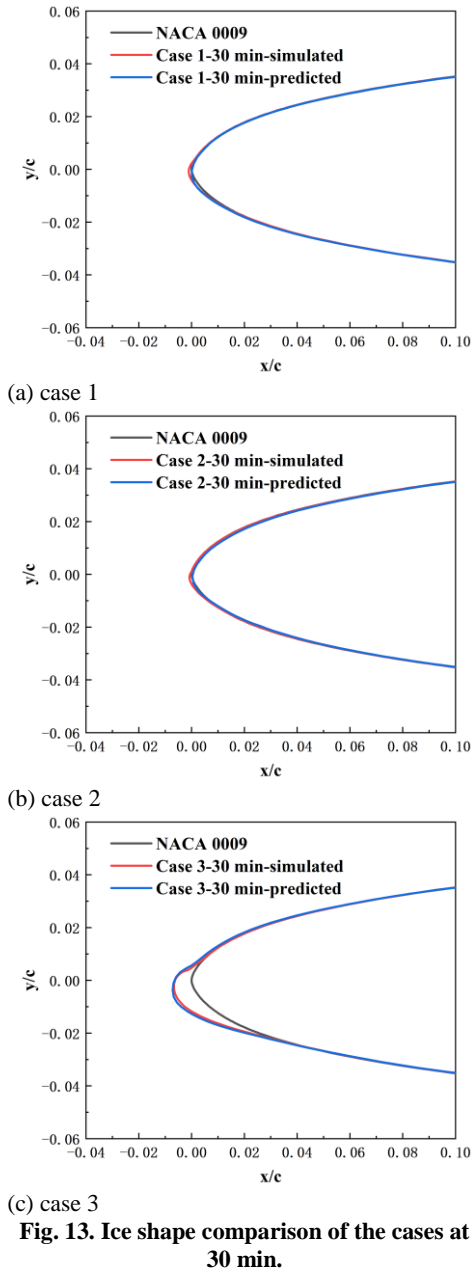


**Fig. 13. Ice shape comparison of the cases at 30 min.**

Figures 14–17 illustrate the ice mass and coefficients of lift, drag, and pitch moment, comparing the predicted results with the numerical simulation and absolute error. The surrogate models accurately predict the parameters related to the iced airfoil at different moments. The maximum relative errors of the ice mass and the coefficients of lift, drag, and pitch moment are 7.8% for case 2 at 30 min, 3.4% for case 2 at 30 min, 3.9% for case 2 at 30 min, and 7.6% for case 2 at 5 min, respectively. A large relative error occurs under the conditions of case 2 because there were fewer sampling conditions near case 2. The prediction accuracy can be improved by adding sampling conditions near case 2.

### 5. CONCLUSIONS

Icing limits the wide application of UAVs. The fast prediction of ice shapes and variation in aerodynamic

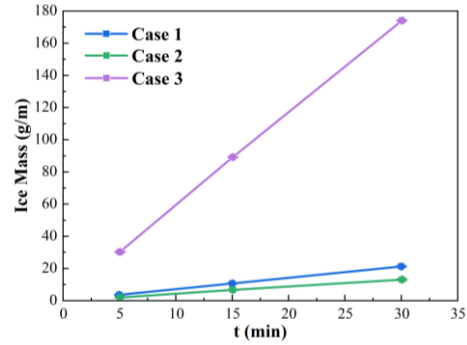


**Fig. 14. Ice mass comparison of surrogate models and the numerical simulation results.**

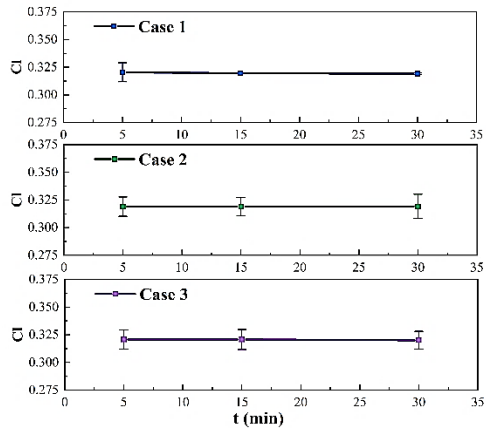


**Fig. 15. Lift coefficient comparison of surrogate models and numerical simulation results.**

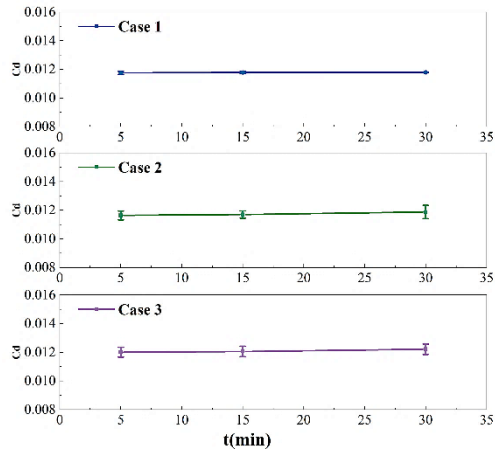


**Fig. 16. Drag coefficient comparison of surrogate models and numerical simulation results.**

characteristics is beneficial to UAV safety. Herein, 80 samples were obtained by OLHS, and the ice accretions and aerodynamic characteristics of the iced configuration were numerically simulated for 5, 15, and 30 min to obtain the ice shape, ice mass, and coefficients of lift, drag, and pitch moment at different times. Based on POD and kriging methods, surrogate models were constructed for the ice shape, ice mass, and aerodynamic coefficients at different times. The results demonstrate that the ice shape predicted by the surrogate model is consistent with

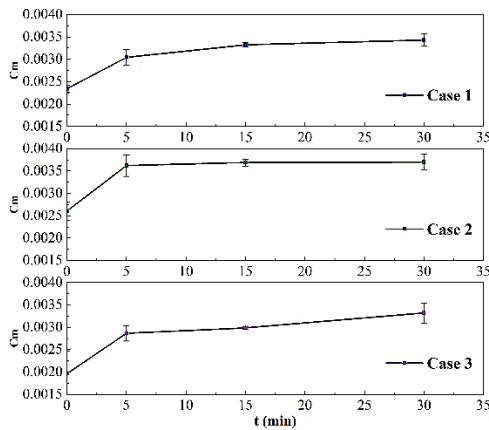


**Fig. 17. Pitch moment coefficient comparison of surrogate models and numerical simulation results.**

the results obtained by numerical simulations. The maximum relative error of ice mass predicted by the surrogate model is 7.8%, and the maximum relative errors of the lift, drag, and pitch moment coefficients are 3.4%, 3.9%, and 7.6%, respectively. The results indicate that the surrogate model based on POD and kriging methods can quickly and accurately predict the changes in the ice shape, ice mass, and aerodynamic characteristics at different times. This is beneficial to the flight safety of UAVs under icing conditions.

#### ACKNOWLEDGMENT

This work benefited greatly from the support of the National Key Project of China under grant GJXM92579 and the Open Fund of Key Laboratory of Icing and Anti/De-icing of China under grant IADL20200101.

#### REFERENCES

Berkooz, G., P. Holmes and J. L. Lumley (1993). The Proper Orthogonal Decomposition in the Analysis of Turbulent Flows. *Annual Review of Fluid Mechanics* 25(1), 539–575.

Bhola, R., N. H. Krishna, K. N. Ramesh, J. Senthilnath and G. Anand (2018). Detection of the power lines in UAV remote sensed images using spectral-spatial methods. *Journal of Environmental Management* 206(15), 1233–1242.

Bourgault, Y., H. Beaugendre and W. G. Habashi (2000). Development of a shallow-water icing model in FENSAP-ICE. *Journal of Aircraft* 37(4), 640–646.

Bragg, M. B., T. Basar T, W. R. Perkins, M. S. Selig, P. G. Voulgaris and J. W. Melody (2002). Smart icing systems for aircraft icing safety. *40th AIAA Aerospace Sciences Meeting & Exhibit AIAA-2002-0813*.

Bragg, M. B. and W. J. Coirier (1986). Aerodynamic measurements of an airfoil with simulated glaze ice. *24th AIAA Aerospace Sciences Meeting*

AIAA-86-0484.

Cebeci, T. and F. Kafyke (2003). Aircraft icing. *Annual Review of Fluid Mechanics* 35(1), 11–21.

Gui, Y. W., Z. H. Zhou, Y. H. Li and H. J. Xu (2017). Multiple safety boundaries protection on aircraft icing. *Acta Aeronautica et Astronautica Sinica* 38(2), 520723.

Han, Z. H. (2016). Kriging surrogate model and its application to design optimization: A review of recent progress. *Acta Aeronautica et Astronautica Sinica* 37(11), 3197–3225.

He, H., G. R. Zhu, C. He and G. P. Chen (2014). Crashworthiness optimization based on Kriging metamodeling. *Journal of Nanjing University of Aeronautics & Astronautics* 46(2), 297–303.

Hossain, K. N., V. Sharma, M. B. Bragg and P. G. Voulgaris (2003). Envelope protection and control adaptation in icing encounters. *Proceedings of the Aiaa Aerospace Sciences Meeting & Exhibit AIAA-2003-25*.

Idris, M. K., J. Qiu, G. W. Melenka and G. Grau (2020). Printing electronics directly onto carbon fiber composites: unmanned aerial vehicle (UAV) wings with integrated heater for de-icing. *Engineering Research Express* 2(2), 025022.

Jaiswal, P., Y. Pasco, G. Yakhina and S. Moreau (2022). Experimental investigation of aerofoil tonal noise at low Mach number. *Journal of Fluid Mechanics* 932, A31.

Jia, Y. Z. (2018). *Investigation of ice ridge forming process and protecting method*. Ms. D. thesis, the Northwestern Polytechnical University, Xi'an, China.

Kim, M., E. E. Essel and P. E. Sullivan (2022). Effect of varying frequency of a synthetic jet on flow separation over an airfoil. *Physics of Fluids* 34(1), 015122.

Krige, D. G. (1951). A statistical approach to some basic mine valuation problems on the Witwatersrand. *Journal of the Southern African Institute of Mining and Metallurgy* 52(6), 119139.

Liu, T., D. Li, R. R. Huang and Z. H. Zhang (2019). Ice shape prediction method of aero-icing based on reduced order model. *Journal of Beijing University of Aeronautics and Astronautics* 45(5), 1033–1041.

Makkonen, L. (1981). Estimating intensity of atmospheric ice accretion on stationary structures. *Journal of Applied Meteorology and Climatology* 20(5), 595–600.

Pei, B., H. Xu, Y. Xue, W. Chen and A. Shen (2018). In-flight icing risk prediction and management in consideration of wing stall. *Aircraft Engineering & Aerospace Technology* 90(1), 24–32.

- Pellissier, M. C., W. G. Habashi and A. Pueyo (2012). Optimization via FENSAP-ICE of aircraft hot-air anti-icing systems. *Journal of Aircraft* 48(1), 265-276.
- Potapczuk, M. G. (2013). Aircraft icing research at NASA Glenn research center. *Journal of Aerospace Engineering* 26(2), 260-276.
- Radmanesh, M., B. Sharma, M. Kumar and D. French (2021). PDE solution to UAV/UGV trajectory planning problem by spatio-temporal estimation during wildfires. *Chinese Journal of Aeronautics* 34(5), 601-616.
- Scherer, J., S. Yahyanejad, S. Hayat, E. Yanmaz, T. Andre, A. Khan, V. Vukadinovic, H. Hellwagber and B. Rinner (2015). An autonomous multi-UAV system for search and rescue. *Proceedings of the First Workshop on Micro Aerial Vehicle Networks, Systems, and Applications for Civilian Use*. 33-38.
- Sharma, V., P. G. Voulgaris and E. Frazzoli (2004). Aircraft autopilot analysis and envelope protection for operation under icing conditions. *Journal of Guidance Control & Dynamics* 27(3), 454-465.
- Shin, J. and T. Bond (1992). Results of an icing test on a NACA 0012 airfoil in the NASA Lewis icing research tunnel. *30th Aerospace Sciences Meeting and Exhibit*. AIAA-1992-647.
- Sirovich, L. (1987). Turbulence and the dynamics of coherent structures I-Coherent structures, II-Symmetries and transformations, III-Dynamics and scaling. *Quarterly of Applied Mathematics* 45(3), 561-571.
- Smith, W. L. (1929). Weather problems peculiar to the New York-Chicago airway. *Monthly Weather Review* 57(12), 503-506.
- Thompson, G. (2019). High Resolution Numerical Weather model forecasts of icing at the ground and in the air. *Proceeding. Int. Workshop on Atmospheric Icing of Structures*, Reykjavík, Iceland, IWAIS.
- Vukits, T. J. (2002). Overview and risk assessment of icing for transport category aircraft and components. *40th AIAA Aerospace Sciences Meeting and Exhibit*, AIAA-2002-0811.
- Wang, M., J. Su, T. Li, X. Wang, Q. Ji, Y. Cao, L. Lin and Y. Liu (2018). Determination of Arctic melt pond fraction and sea ice roughness from Unmanned Aerial Vehicle (UAV) imagery. *Advances in Polar Sciences* 29(3), 181-189.
- Yao, S. B., D. L. Guo, Z. X. Sun, G. W. Yang and D. W. Chen (2013). Multi-objective optimization of the streamlined head of high-speed trains based on the kriging model. *Science China* 43(2), 186-200.
- Zeppetelli, D. and W. G. Habashi (2012). In-flight icing risk management through computational fluid dynamics-icing analysis. *Journal of Aircraft* 49(2), 611-621.